



183rd Meeting of the Acoustical Society of America

Nashville, Tennessee

5-9 December 2022

Musical Acoustics: Paper 2aMU1

Low-frequency directional characteristics of a gamelan gong

Samuel David Bellows, Dallin T. Harwood, Kent L. Gee and Timothy W. Leishman

Department of Physics and Astronomy, Brigham Young University, Provo, UT, 84602;

samuel.bellows11@gmail.com; dallinharwood@gmail.com; kentgee@byu.edu; tim.leishman.byu@gmail.com

The structural modes of gamelan gongs often have clear impacts on their far-field directivity patterns with the number of directional lobes corresponding to the associated structural mode shapes. Many of the lowest modes produce dipole-like radiation with the dipole moment determined by the positions of the nodal and antinodal regions. Spherical harmonic and multipole expansions facilitate further understanding of the gongs' low-frequency directional characteristics. The expansions also yield practical simplifications to model their radiation.

1. INTRODUCTION

Measured directivity patterns are valuable resources to characterize the sound radiation from musical instruments. They have additional applications in room acoustical designs,^{1,2} auralizations,^{3,4} and microphone placements.⁵ While research has provided some understanding of the directional characteristics of Western orchestral instruments,^{1,6–9} there remains much less understanding, with notable exceptions,^{2,10,11} regarding the radiation of instruments from other music cultures.

The structural acoustics of Indonesian gamelan gongs have received considerable attention due to their unique characteristics. Due to his interest in the tuning procedure of gamelan gongs, McLachlan¹² measured the acoustic outputs of gongs made of different materials. He found that the boss (hemispherical dome at the gong's center) beaten into the gong's face raised its fundamental frequency, whereas thinning lowered the frequency. His finite-element method (FEM) models illustrated how the boss shape, gong rim thickness, and rim angle all modified and tuned modal frequencies.

Krueger et al.¹³ investigated *ombak*, an acoustic beating phenomenon of a large ageng wadon Balinese gamelan gong. Both acoustical and scanning laser Doppler vibrometer (SLDV) measurements identified its lowest modal frequencies. Despite the agreement between the acoustic and structural measurements, the researchers found that the acoustic signal contained frequency peaks near the sum and difference frequencies of the first gong axial modes. They additionally discovered second and third harmonics of the fundamental axial mode that suggested significant nonlinear effects. Subsequent measurements using increasing excitation force confirmed that nonlinear interactions between the modes were a primary cause of *ombak*.

Perrin et al.¹⁴ studied a small gamelan gong. Their analysis employed finite-element method (FEM) modeling, electronic speckle pattern interferometry (ESPI), and SLDV scans to tabulate its modal frequencies. Although discrepancies in the modal frequencies arose between the measurement modalities, the authors generally found that the “modified Chladni’s law” gave predictions in good agreement with the ESPI data. They confirmed nonlinear behavior and identified three modes as the most acoustically significant: the radial (0, 1) mode and the pair of angular-radial (1, 1) modes.

While many studies have thus provided more knowledge regarding the structural modes of gamelan gongs, their acoustic radiation patterns have remained unclear. Zotter¹⁰ measured the directivity of an ageng gamelan gong using a 10-channel microphone array and assuming axial symmetry. He found dipole-like directivity for the first two axial modes of the instrument. He also included results for time-varying directivities due to beating effects. However, the symmetry assumption limited the analysis to only two modes.

This work presents the directivity patterns of an ageng lanang Balinese gamelan gong assessed by a high-resolution spherical directivity measurement system. Subsequent SLDV scans revealed close connections between the gong’s far-field radiated patterns and mode shapes. Similar to Zotter’s results, the directivities reveal dipole-like radiation at the lowest frequencies. At higher frequencies, the sound radiation takes on more complex patterns. Spherical harmonic and subsequent multipole expansions allow equivalent point source representations of the gong’s acoustic radiation at the lowest frequencies.

2. METHODS

A. MEASUREMENTS

As shown in Fig. 1, a rotating semicircular microphone array assessed the directivity of the ageng lanang gamelan gong. The microphone array consisted of 36 12.7 mm (0.5 in) precision microphones spaced in 5° degree increments in the polar angle. Array rotations in 5° azimuthal steps allowed a full spherical scan of 2,521 unique sampling positions, consistent with the AES directivity sampling standard,¹⁵ with the omission of the nadir position.



Figure 1: An ageng lanang gamelan gong within the rotating directivity measurement array.

A swept-sine input signal sent to a shaker excited the gong over the audible bandwidth. Several measurements employed varying shaker contact points to ensure the excitation of numerous normal modes of vibration. A near-field reference microphone provided a directivity input signal for calculating frequency response functions (FRFs) between it and the output of each array microphone signal. While the shaker input excitation signal is notably more repeatable than that of played musical instruments,⁸ FRFs nonetheless increase extraneous noise immunity and provide a convenient normalization to address any variations that might occur between measurement rotations.

To better understand how the gong's modal shapes influenced its directivity, additional measurements followed from an SLDV scan of the instrument. As for the directivity measurements, the shaker excited the instrument while the laser head scanned 977 positions on the gong's front face. The spatial resolution allowed modal analysis well above 1.5 kHz, although this work primarily focuses on results for lower frequencies.

B. SIGNAL PROCESSING

The directivity near-field input autospectrum $G_{aa,v}$ for the v^{th} rotation and the FRF H_{uv} for the u^{th} array microphone and v^{th} rotation followed from standard spectral estimation and deconvolution procedures.^{16,17} The effective input autospectrum,¹⁸

$$G_{aa,\text{eff}}(f) = \frac{\sum_{u=0}^{U-1} \sum_{v=0}^{V-1} w_{uv} G_{aa,v}(f) |H_{uv}(f)|^2}{\sum_{u=0}^{U-1} \sum_{v=0}^{V-1} w_{uv} |H_{uv}(f)|^2}, \quad (1)$$

where w_{uv} are quadrature weights for numerical integration over the sphere,^{19,20} yielded an averaged input autospectrum over the azimuthal rotations. The total effective time-averaged sound power^{16,21} radiated by

the gong was

$$\langle W(f) \rangle_{t,eff} = R^2 \frac{G_{aa,eff}(f)}{\rho_0 c} \sum_{u=0}^{U-1} \sum_{v=0}^{V-1} w_{uv} |H_{uv}(f)|^2, \quad (2)$$

where R is the measurement radius. Peak extraction of $\langle W(f) \rangle_{t,eff}$ allowed determination of the gong's modal frequencies from the acoustic signals.

C. SPHERICAL HARMONIC EXPANSIONS

The spherical harmonics provide an orthonormal basis for expanding directivities over the spherical evaluation surface.^{10,22} As the angular component of the Helmholtz-equation solution on the exterior domain, they find important applications in wave-based modeling of sound fields.²³ The normalized spherical harmonics of degree n and order m are defined here as²⁴

$$Y_n^m(\theta, \phi) = \sqrt{\frac{2n+1}{4\pi} \frac{(n-m)!}{(n+m)!}} P_n^m(\cos \theta) e^{im\phi}, \quad (3)$$

where P_n^m are the associated Legendre functions of degree n and order m .

The pressure field for $r \geq R$ is²³

$$p(r, \theta, \phi, k) = \sum_{n=0}^{\infty} \sum_{m=-n}^n c_n^m(k) h_n^{(2)}(kr) Y_n^m(\theta, \phi), \quad r \geq R, \quad (4)$$

where $h_n^{(2)}(kr)$ are the spherical Hankel functions of the second kind (for outward propagation and $e^{i\omega t}$ time dependence). The expansion coefficients follow by exploiting the spherical harmonic's orthogonality over the sphere:

$$c_n^m(k) = \frac{1}{h_n^{(2)}(kR)} \int_0^{2\pi} \int_0^\pi p(R, \theta, \phi, k) [Y_n^m(\theta, \phi)]^* \sin \theta d\theta d\phi, \quad (5)$$

where * indicates complex conjugation. Numerical quadrature allows evaluation of the integral.²⁰ Once determined, the expansion coefficients allow computation of extrapolated far-field directivities via the large-argument representations of the spherical Hankel functions:²¹

$$D_{ff}(\theta, \phi) = \sum_{n=0}^{\infty} \sum_{m=-n}^n c_n^m(k) i^n Y_n^m(\theta, \phi). \quad (6)$$

Extrapolation of the complex pressure also allows far-field corrections for the sound power estimate when R is in the near-field of the source.

D. MULTIPOLE REPRESENTATION

A multipole expansion of the Kirchhoff Helmholtz Integral Equation (KHIE) yields a simplified representation of the source's sound field.^{21,25} The monopole moment is²¹

$$M = \iint_S iz_0 k u_n(\mathbf{r}) dS \quad (7)$$

and the dipole moment is

$$\mathbf{D} = \iint_S [iz_0 k \mathbf{r} u_n(\mathbf{r}) + \hat{\mathbf{n}} p(\mathbf{r})] dS, \quad (8)$$

where u_n and p are the normal velocity and pressure on the radiating body's boundary surface S , respectively. At low-frequencies and neglecting higher order moments (e.g. quadrupole), the resultant field becomes

$$p(\mathbf{r}) \approx p_m(\mathbf{r}) + p_d(\mathbf{r}), \quad (9)$$

where

$$p_m(\mathbf{r}) = M \frac{e^{-ikr}}{4\pi r} \quad (10)$$

is the monopole field and

$$p_d(\mathbf{r}) = ik \frac{e^{-ikr}}{4\pi r} \left(1 + \frac{i}{kr} \right) \mathbf{D} \cdot \hat{\mathbf{r}} \quad (11)$$

is the dipole field.

One may use the spherical harmonic expansion coefficients to infer the multipole moments of the source.^{23,26,27} For example, the following matrix equation converts the degree $n = 0$ and $n = 1$ expansion coefficients into the monopole and dipole moments:

$$\begin{bmatrix} M \\ D_x \\ D_y \\ D_z \end{bmatrix} = \frac{i\sqrt{\pi}}{k^2} \begin{bmatrix} 2k & 0 & 0 & 0 \\ 0 & \sqrt{6} & 0 & -\sqrt{6} \\ 0 & -i\sqrt{6} & 0 & -i\sqrt{6} \\ 0 & 0 & 2\sqrt{3} & 0 \end{bmatrix} \begin{bmatrix} c_0^0 \\ c_1^{-1} \\ c_1^0 \\ c_1^1 \end{bmatrix}. \quad (12)$$

The matrix entries result from equating the multipole and spherical harmonic expansion terms.²³ However, only in the limit of $kR \ll 1$ do the derived multipole moments correspond to the integrals in Eqs. (7) and (8).²⁸

Notably, the known monopole and dipole moments of the gong allow a representation of the sound field using an equivalent point-source model.²⁶ Such models are often more convenient for numerical simulations using directivities.²⁹ Figure 2 illustrates the locations and amplitudes of a seven-point-source model that reconstructs the pressure field for $kR \ll 1$ with high accuracy provided that $k\epsilon \ll 1$, where ϵ is the separation distance of opposing point sources. The single point source at the origin represents the monopole field, whereas the three orthogonal opposite-polarity pairs represent the dipole field. Consequently, one may readily construct a low-frequency equivalent point source representation of a source once its spherical harmonic expansion coefficients are known.

3. RESULTS

A. MODAL EXTRACTION

Figure 3 shows an example of the normalized $\langle W(f) \rangle_{t,\text{eff}}$ radiated by the gong when excited by the shaker, plotted as a function of both frequency dimensionless ka , where $a = 0.4$ m is the gong's radius. As anticipated, the instrument's modal nature strongly characterizes its acoustic output. Below 200 Hz, eight sharp, distinct peaks evidence the gong's lowest modes. The spectral region from 200 Hz to around 350 Hz appears as a gap with no strongly radiating modes. Increased modal density occurs above 350 Hz, although the radiated level is generally lower than for the lowest eight modes.

Figure 4 plots the surface velocity of the gong as measured by the SLDV for the frequencies of the eight lowest modal peaks. Additionally, Table 1 reports the corresponding modal frequencies as extracted acoustically from the microphone output and structurally from the SLDV measurements. The two measurement modalities produced excellent agreement for the extracted modal frequencies; only the $(0, 1)$ mode had a 1 Hz discrepancy in its value.

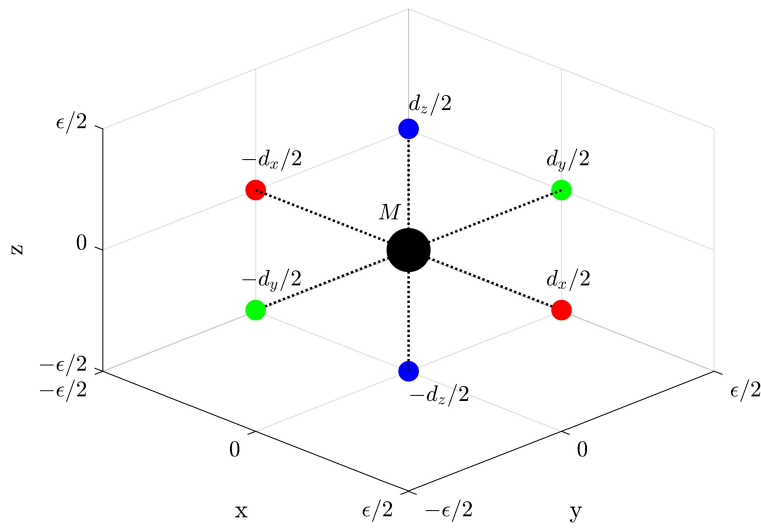


Figure 2: Source locations, amplitudes, and polarities for an equivalent point source model involving seven point sources.

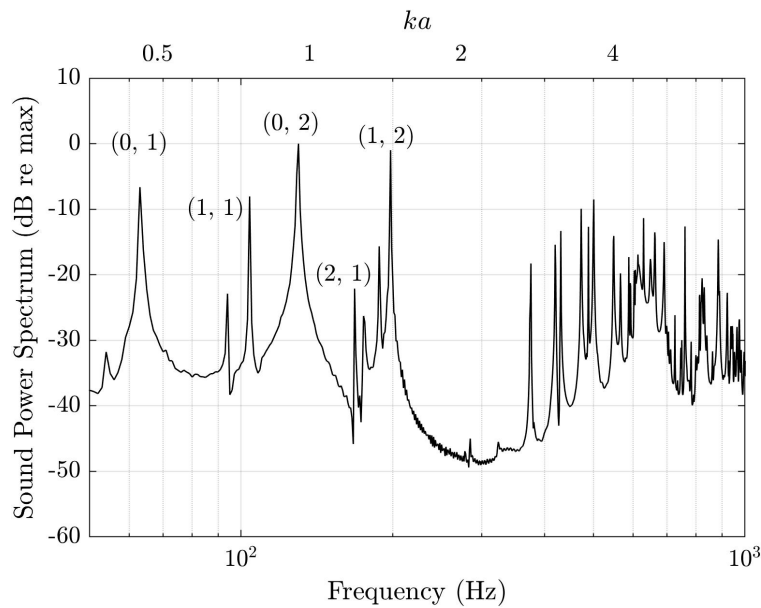


Figure 3: Normalized effective time-averaged sound power spectrum radiated from the gong when excited by a shaker.

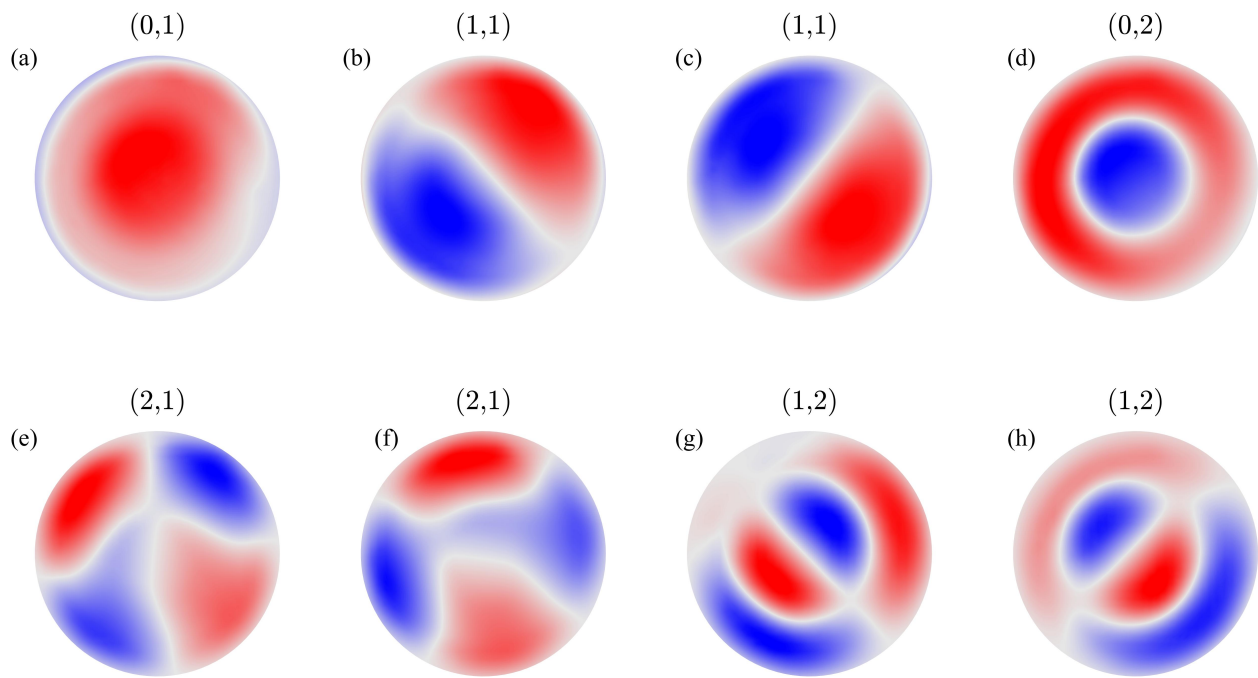


Figure 4: Normalized out-of-plane gong surface velocity at the sound power spectral peaks based on SLDV scan data and assumed modal numbers. (a) 63 Hz. (b) 94 Hz. (c) 104 Hz. (d) 130 Hz. (e) 168 Hz. (f) 175 Hz. (g) 188 Hz. (h) 198 Hz.

Table 1: Lowest eight modal frequencies of the gong and assumed modal numbers.

Frequency (Acoustic)	Frequency (SLDV)	Angular	Radial
63	64	0	1
94	94	1	1
104	104	1	1
130	130	0	2
168	168	2	1
174	174	2	1
188	188	1	2
198	198	1	2

Perrin et al.¹⁴ identified the (0, 1) and (1, 1) modes as being among the most acoustically significant for small gamelan gongs. These mode shapes for the ageng lanang gamelan gong used in the present work appear in Figs. 4(a) through 4(c) and occur at 63 Hz, 94 Hz, and 104 Hz, respectively. From the radiated sound power spectrum shown in Fig. 3, both the 63 Hz (0, 1) mode and the 104 Hz (1, 1) mode radiate at similar levels. The reduced level for the 94 Hz (1, 1) mode may have been caused by the stinger placement, as the nodal lines were unknown before the measurements.

Krueger et al.¹³ determined that the nonlinearly generated harmonics of the (0, 1) mode interacting with the (0, 2) mode create ombak for some large gamelan gongs. Thus, the (0, 2) mode should be acoustically significant in addition to the (0, 1) and (1, 1) modes identified by Perrin et al. Its mode shape appears in Fig. 4(d) and has a modal frequency of 130 Hz. Its radiated sound power level shown in Fig. 3 is the highest of all modes, confirming its importance to the gong's overall sound.

The next highest modes in Table 1 are the two (2, 1) modes at 168 and 174 Hz. However, from the radiated sound power curves, these modes do not appear to radiate efficiently compared to the other low-frequency modes. Their relatively weak radiation contrasts with the two strongly radiating (1, 2) modes occurring at 188 Hz and 198 Hz. The level of the 198 Hz (1, 2) mode is within 1 dB of the (0, 2) mode's level.

B. DIRECTIVITY RESULTS

Figure 5 shows the propagated and normalized far-field directivities for the lowest eight modes, where both color and balloon radius indicate the relative levels on a 40 dB scale. The gong faced the 0° degree azimuthal angle marker during the measurements.

As seen in Figs. 5(a) through 5(c), the directivity is dipolar for the (0, 1) and (1, 1) modes. For the (0, 1) mode, the out-of-phase velocities of the front and back gong faces produce a dipole moment in the x -direction (towards the 0° azimuthal marker). The (1, 1) modal patterns in Fig. 4 have node lines on the gong surface that approximately define the far-field directivity nulls. The velocity distribution on the front face of the gong determines the dipole moment in roughly the positive y - z -direction for the 94 Hz (1, 1) mode and the negative y - z -direction for the 104 Hz (1, 1) mode. Given that the surface velocity distribution on the back face of the gong has opposite polarity to the distribution on the front face, it is somewhat surprising that these modes do not form an angled lateral quadrupole.

The dominant (0, 2) mode shown in Fig. 5(d) also has dipole-like directivity, but its null is not as well defined. The effect is possibly due to an increasing monopole moment.²⁸ Zotter¹⁰ also observed dipole-like directivity for the (0, 1) and (0, 2) modes, although his symmetry assumptions did not allow identification of the dipolar nature of the (1, 1) modes.

The directivity at the next four modal peaks, shown in Figs. 5(e) through 5(h), have more complex directivity patterns with regions of strong and weak radiation. The directivity at the 168 Hz modal peak has more omnidirectional-like radiation except for a null running along the direction of the gong's right side. The directivity at the 175 Hz modal peak has a null dividing the most substantial radiation between the positive and negative x - z directions. The directivity at the 188 Hz modal peak is similar to that of the 94 Hz (1, 1) mode. Comparison of the out-of-plane velocity distribution of these two modes in Figs. 4(b) and 4(g) confirms that the location of the angular node line falls at a similar position on the gong's face. However, for the directivity at the 198 Hz modal peak is not similar to that of its corresponding 104 Hz (1, 1) mode.

C. LOW-FREQUENCY MODELING

The gong's lowest four modes fall in the frequency regime corresponding to $ka < 1$. Additionally, the far-field directivities suggest that only a monopole and dipole field may reasonably represent the lowest four

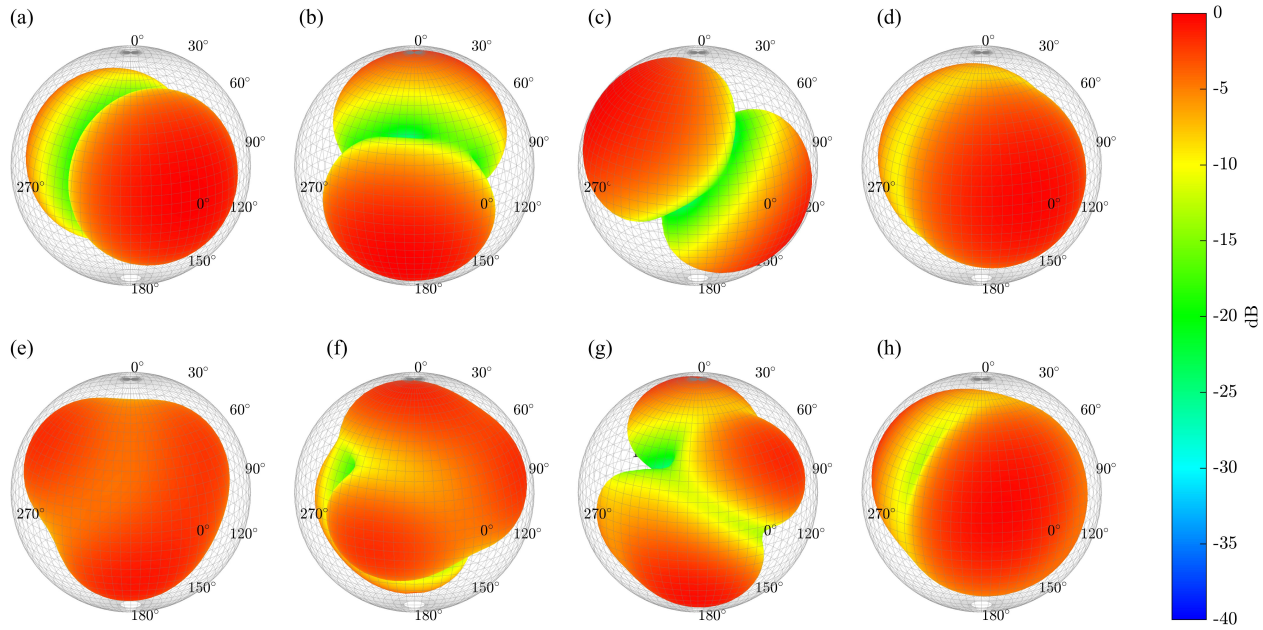


Figure 5: Propagated and normalized far-field directivities for the gong’s lowest eight modal frequencies: (a) 63 Hz, (b) 94 Hz, (c) 104 Hz, (d) 130 Hz, (e) 168 Hz, (f) 175 Hz, (g) 188 Hz, and (h) 198 Hz.

modes. The next four modes have more complex surface velocity distributions and far-field patterns; thus, higher-order moments may be necessary to model their fields adequately.

Figure 6 shows the far-field directivity for each gong mode based on a superposition of the monopole and dipole fields. Comparisons with the measured far-field directivities in Fig. 5 reveals good agreement for the lowest four mode. In each case, the direction of radiation lobes and nulls align. For the higher four modes, the agreement is not as good. While some general qualitative features remain, there are discrepancies in the locations and strengths of the various lobes and nulls.

An area-weighted directivity factor function deviation quantifies the differences between the measured and modeled propagated far-field patterns as a single level L_Q .³⁰ Figure 7 shows the value of L_Q for each mode. The deviations for the lowest four modes remain below 1.0 dB, again showing that they tend to have the best agreement. The deviations for the higher four modes are larger, approaching values closer to 3 dB. Consequently, for $ka > 1$, the accuracy declines for multipole representations using only the monopole and dipole fields.

4. CONCLUSIONS

The structural mode shapes of the gamelan gong often have close connections to their far-field directivity patterns. The ageng lanang Balinese gamelan gong measured in this work has a set of eight modes over 150 Hz bandwidth spanning the musical notes B1 to G3 (20 semitones). Above this region, a 150 Hz band gap occurs. A spectral regime with increasing modal densities follows this gap.

The surface velocity distributions and nodal lines of the lowest four modes allow qualitative predictions of dipole-like far-field directivity patterns. Multipole expansions using only monopole and dipole fields represent the gong’s radiation patterns for these modes with high accuracy. However, higher modes take on more complex patterns that are more difficult to represent with only two contributing field types.

This work only considered the modeling of gong directivity patterns with monopole and dipole fields. Future research could include higher-order (e.g., quadrupole) fields or applying more general equivalent

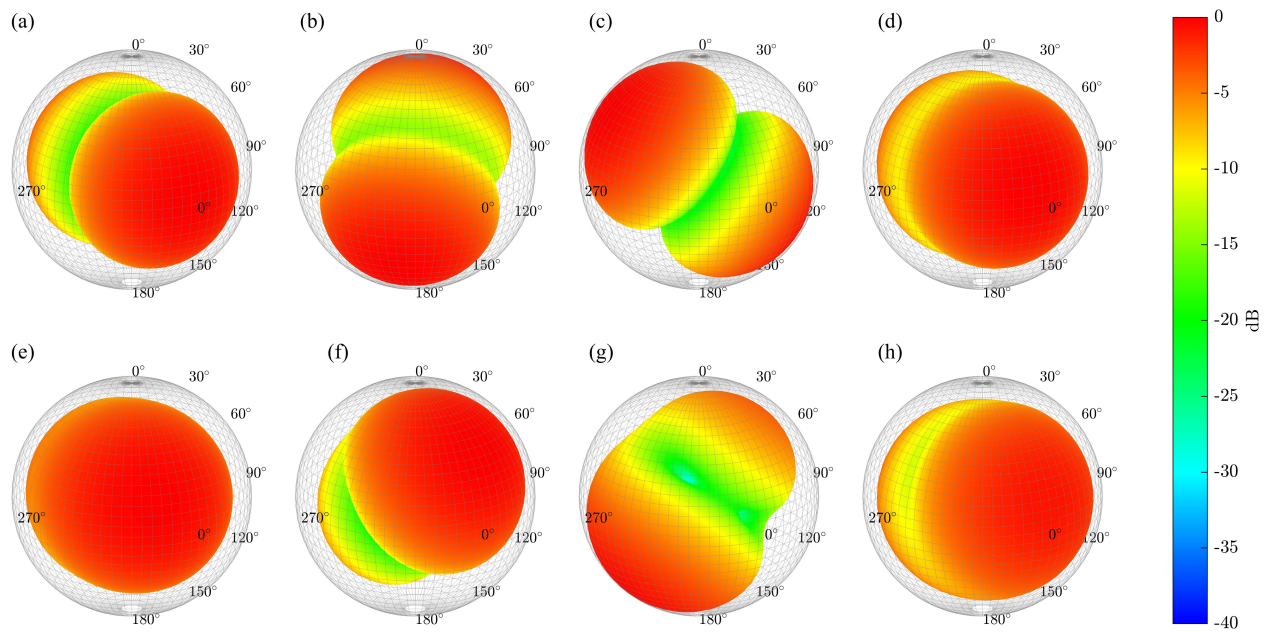


Figure 6: Simulated far-field gong directivities based on superpositions of monopole and dipole fields for the modal frequencies (a) 63 Hz, (b) 94 Hz, (c) 104 Hz, (d) 130 Hz, (e) 168 Hz, (f) 175 Hz, (g) 188 Hz, and (h) 198 Hz.

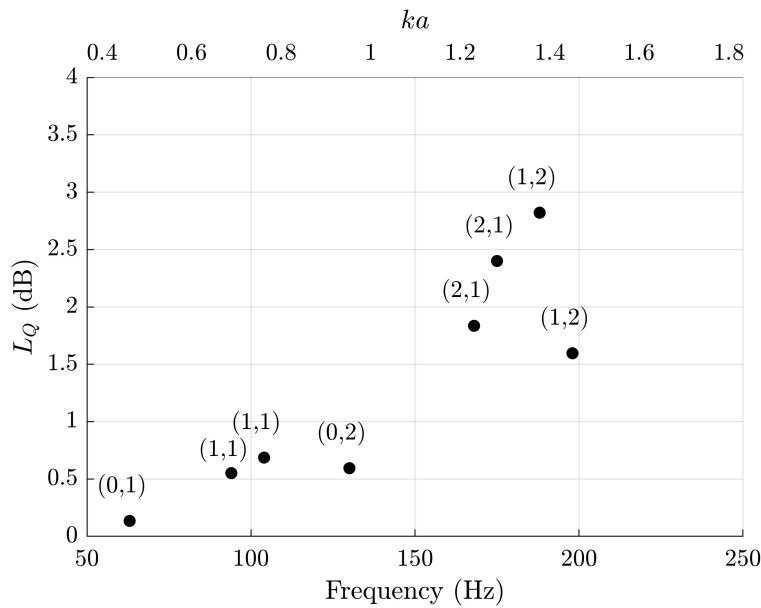


Figure 7: Area-weighted directivity factor function deviations L_Q between simulated and propagated far-field patterns for the lowest eight modes.

point source methods. Considering the radiation from nonlinearly excited modes would provide a better understanding of the gong's acoustic radiation under normal playing conditions. Another interesting area of future research might include comparing the behaviors of other gongs to gain insights into how the results of this work generalize to other ensemble instruments.

ACKNOWLEDGMENTS

The authors express appreciation for funding from the William James and Charlene Fuhriman Strong Family Musical Acoustics Endowed Fellowship Fund, to Dr. Jeremy Grimshaw for lending the gongs for measurements, and to Dr. Micah Shepherd for his insightful comments.

REFERENCES

- ¹ J. Meyer, "The sound of the orchestra," *J. Audio Eng. Soc.*, **41**(4), pp. 203–213, 1993.
- ² C. H. Jeong, J. G. Ih, C. H. Yeon, and C. H. Haan, "Prediction of the acoustic performance of a music hall considering the radiation characteristics of korean traditional musical sources," *J. Kor. Acoust. Soc.*, **23**(2), pp. 146–161, 2004.
- ³ F. Otundo and J. H. Rindel, "A new method for the radiation representation of musical instruments in auralizaitons," *Acta Acustica united with Acustica*, **91**, pp. 902–906, 2005.
- ⁴ M. C. Vigeant, L. M. Wang, and J. H. Rindel, "Investigations of orchestra auralizations using the multi-channel multi-source auralization technique," *Acta Acustica united with Acustica*, **94**, pp. 866–882, 2008.
- ⁵ M. Clark Jr. and P. Minter, "Dependence of timbre on the tonal loudness produced by musical instruments," *J. Audio Eng. Soc.*, **12**(1), 1964.
- ⁶ H. F. Olson, *Musical Engineering: An Engineering Treatment of the Interrelated Subjects of Music, Musical Instruments, Speech, Acoustics, Sound Reproduction and Hearing*. New York: McGraw-Hill, 1952.
- ⁷ J. Pätynen and T. Lokki, "Directivities of symphony orchestra instruments," *Acta acustica united with acustica*, **96**, pp. 138–167, 2010.
- ⁸ K. J. Bodon, "Development, evaluation, and validation of a high-resolution directivity measurement system for played musical instruments," Master's thesis, Brigham Young University, 2016.
- ⁹ S. Weinzierl, M. Vorländer, G. Behler, F. Brinkmann, H. v. Coler, E. Detzner, J. Krämer, A. Lindau, M. Pollow, F. Schulz, and N. R. Shabtai, "A database of anechoic microphone array measurements of musical instruments," 2017.
- ¹⁰ F. Zotter, "Analysis and synthesis of sound-radiation with spherical arrays," Doctoral dissertation, Institute of Electronic Music and Acoustics University of Music and Performing Arts, 2009.
- ¹¹ H. Ghasemi, "Directivity measurement of santur instrument," in *Proceedings of the 19th International Congress on Sound and Vibration*, (Vilnius, Lithuania), pp. 3120–3124, 2012.
- ¹² N. McLachlan, "Finite element analysis and gong acoustics," *Acoustics Australia*, **25**(3), p. 103–107, 1997.
- ¹³ D. W. Krueger, K. L. Gee, and J. Grimshaw, "Acoustical and vibrometry analysis of a large balinese gamelan gong," *J. Acoust. Soc. Am.*, **128**(1), pp. EL8–EL13, 2010.

- ¹⁴ R. Perrin, D. P. Elford, L. Chalmers, G. M. Swallowe, T. R. Moore, S. Hamdan, and B. J. Halkon, “Normal modes of a small gamelan gong,” *J. Acoust. Soc. Am.*, **136**(4), pp. 1942–1950, 2014.
- ¹⁵ AES56-2008 (r2014): *AES Standard on Acoustics: Sound Source Modeling: Loudspeaker Polar Radiation Measurements* (Audio Engineering Society, New York, 2015).
- ¹⁶ J. S. Bendat and A. G. Piersol, *Random Data: Analysis and Measurement Procedures*. Wiley, Hoboken, NJ, 4 ed., 2010.
- ¹⁷ A. J. Berkhouit, “A new method to acquire impulse responses in concert halls,” *J. Acoust. Soc. Am.*, **68**, p. 179, 1980.
- ¹⁸ T. W. Leishman, S. D. Bellows, C. M. Pincock, and J. K. Whiting, “High-resolution spherical directivity of live speech from a multiple-capture transfer function method,” *J. Acoust. Soc. Am.*, **149**(3), pp. 1507–1523, 2021.
- ¹⁹ S. D. Bellows and T. W. Leishman, “Spherical harmonic expansions of high-resolution musical instrument directivities,” *Proc. Mtgs. Acoust.* **35**, 035005, 2018.
- ²⁰ J. R. Driscoll and D. M. Healy, “Computing fourier transforms and convolutions on the 2-sphere,” *Advances in Applied Mathematics*, **15**, pp. 202–250, 1994.
- ²¹ A. D. Pierce, *Acoustics*. Springer International Publishing, 2019.
- ²² R. Kennedy and P. Sadeghi, *Hilbert Space Methods in Signal Processing*. Cambridge University Press, 2013.
- ²³ E. G. Williams, *Fourier Acoustics: Sound Radiation and Nearfield Acoustical Holography*. London: Academic Press, 1999.
- ²⁴ T. M. Dunster, *NIST Handbook of Mathematical Functions*. New York: Cambridge University Press, 2010.
- ²⁵ A. Chaigne and J. Kergomard, *Acoustics of Musical Instruments*. Springer New York, 2016.
- ²⁶ T. Martin and A. Roure, “Optimization of an active noise control system using spherical harmonics expansion of the primary field,” *J. Sound Vib.*, **201**(5), pp. 577–593, 1997.
- ²⁷ B. M. Shafer, “Error Sensor Placement for Active Control of an Axial Cooling Fan,” Master’s thesis, Brigham Young University, 2007.
- ²⁸ G. Weinreich, “Sound hole sum rule and the dipole moment of the violin,” *J. Acoust. Soc. Am.*, **77**(2), pp. 710–718, 1985.
- ²⁹ J. Escolano, J. J. López, and B. Pueo, “Directive sources in acoustic discrete-time domain simulations based on directivity diagrams,” *J. Acoust. Soc. Am.*, **121**(6), pp. EL256–EL262, 2007.
- ³⁰ S. Bellows and T. W. Leishman, “Effect of Head Orientation on Speech Directivity,” in *Proc. Interspeech 2022*, pp. 246–250, 2022.